



Tuning of lattice thermal conductivity of amorphous $\text{Fe}_{0.85}\text{Zr}_{0.15}$ by nanostructured voids, pressure and temperature

Emel Gürbüz, Biplab Sanyal *

Division of Materials Theory, Department of Physics and Astronomy, Box 516, Uppsala University, SE-751 20 Uppsala, Sweden

ARTICLE INFO

Keywords:

Metallic glass
Thermal conductivity
Molecular dynamics simulations
Density functional theory
Voronoi
Vibrational properties

ABSTRACT

Metallic glasses are known as one of the favorable amorphous materials with their remarkable stiffness, durability and low thermal conductivities. Furthermore, manipulation of lattice thermal conductivity by forming nanostructures is an important route to enhance the performance for several industrial applications. Here, equilibrium molecular dynamics simulations were performed for the generation of metallic glass (MG) $\text{Fe}_{0.85}\text{Zr}_{0.15}$ followed by the calculation of lattice thermal conductivity by Green–Kubo method. The amorphicity of our simulated MG is verified through the analysis of radial distribution functions and Voronoi tessellations. Nanostructured spherical voids with varying sphere radii were introduced. We have found that with increasing porosity, the lattice thermal conductivity decreases. We have also studied the dependence of temperature and pressure on thermal conductivity. Finally, our analysis of calculated vibrational densities of states shows interesting behavior of extended and localized modes in various situations of pressure, temperature and size of the nanostructured voids.

Amorphous materials, and in particular metallic glasses (MGs), can be attractive alternatives to their crystalline counterparts for industrial applications, such as those involving magnetic cycling where MGs exhibit smaller energy losses [1–3]. One of the most commonly used MGs in industry are zirconium-based MGs. A zirconium-based bulk MG was first produced in the early 1990s by Johnson et al. [4] A major challenge for large-scale production of zirconium-based MGs has been the involved cost. To overcome this issue, zirconium (Zr) was mixed with cheaper ferrous materials such as iron (Fe), nickel (Ni) and chromium (Cr). As a result, these new compounds exhibit increased hardness, strength, higher resistance to corrosion, yet are highly processable at production costs similar to that of stainless steel [5]. MGs have no structural long-range order [6] but they exhibit short-range order (SRO) and medium-range order (MRO) [2]. The SRO in MGs is determined by the elemental composition. Ma et al. identified possible SROs of CuZr MGs as a function of their composition and that the locally favored motif is a full icosahedral structure, which centers around the Cu atom and can be represented with the Voronoi index $\langle 0, 0, 12, 0 \rangle$ [6]. However, it was also shown that in addition, different motifs were formed, interconnecting with each other and constructing the MG.

Thermal conductivity of amorphous materials is an important research topic in solid state physics [7,8]. Amorphous materials exhibit low thermal conductivity relative to crystalline materials because of their strongly localized heat carriers [7,9,10]. Amorphous materials

with low thermal conductivity have a very important place in many applications, for example in wearable electronics, thanks in particular to their flexibility and low thermal conductivity [7,11,12]. The amorphous counterparts of crystalline silicon-based semiconductors are even seen as promising future candidates for next-generation artificial intelligence chips, since they could better cope with the challenging heat dissipation [7,13,14]. Especially, metallic glasses and metallic glassy alloys, which are popular candidates for these applications are known for their low thermal conductivity below 9 W/K m out of which the lattice thermal conductivity was shown to be below 2 W/K m from calculations [15–17].

Low conductors of heat that are lightweight, with excellent mechanical strength and high stiffness, are the most desirable materials to be used as thermal barrier coatings [7,18,19], in particular for space applications [7,20–22]. Materials with low thermal conductivity are also used as thermal coating materials in high-energy particle detectors. Their usage in gamma ray detectors can also improve the sensitivity of the detector [7,23]. Amorphous materials are also becoming increasingly relevant as thermoelectric systems where heat is directly converted to electrical energy and the device efficiency is favored by high electric conductivity and low thermal conductivity [24]. In most applications, the desired lowering of the lattice thermal conductivity is achieved by increasing the scattering of phonons through the introduction of nanostructures and interfaces [7,20,25,26]. Phononic

* Corresponding author.

E-mail address: Biplab.Sanyal@physics.uu.se (B. Sanyal).

crystals, which incorporate periodically arranged nanopillars [27] or nanodots [28] are prominent examples. Similarly, membranes, which are patterned in a variety of shapes [29–36], are further examples that show the structural design effect on the thermal conductivity of the materials. In these studies, it is shown that the structural design backscatters phonons and thus gives rise to non-propagating phonon modes, which decrease the thermal conductivity. Semimetallic and semiconductor glasses can be good candidates for thermoelectric materials [37]. Moreover, Yu et al. have shown that Zr-based thin film metallic glasses with AgSbTe₂ substrate can act as an effective diffusion barrier [16].

In this work, nanostructured voids have been introduced in MG Fe_{0.85}Zr_{0.15} and the variation of thermal conductivity by varying the size of the voids has been studied. This particular composition allows for a Zr content, which is large enough to facilitate reliable formation of the amorphous phase during quenching. In addition, at this composition, Fe–Zr is nonmagnetic [38]. Most commonly, insulators are studied and it is attempted to reduce the thermal conductivity through different techniques. Here, instead, we start with a material that possesses very low thermal conductivity and keep decreasing it by way of nano-engineering (i.e., introducing voids). This can keep a balance between the electronic component and Zr-based metallic glasses' lattice thermal conductivity, which may help to increase the efficiency of thermoelectric modules in which Zr-based metallic glasses are used as thermal barriers for future studies.

The outline of this paper is the following: First, we introduce the computational methods. Second, we discuss our results, where we start with the structural characteristics of the simulated MG followed by the stability of the MGs with the nanostructured voids. Next, we discuss the calculated thermal conductivity as a function of porosity and analyze with the help of a simple classical model. Furthermore, the temperature and pressure dependence of thermal conductivity is shown. Finally vibrational analysis of the structures is presented to discuss the nature of the modes in terms of participation ratio.

1. Methods

Both classical molecular dynamics (CMD) and first-principles MD (FPMD) were performed on the basis of Born–Oppenheimer approximation. For the CMD simulations, we used the Large-scale Atomic/Molecular Massively Parallel Simulator (LAMMPS) [39] code. The embedded atom method (EAM) [40] potentials with many body interactions were used, which are computationally efficient for alloys. The EAM potential used in our study was obtained from fitting experimental data and was parameterized for various physical properties such as enthalpy of formation or mixing, lattice parameter, and elastic constant.

For the FPMD simulations, we used VASP (Vienna ab initio simulation package) [41,42] employing the projector-augmented-wave (PAW) [43] method to describe electron-ion interaction. The electron exchange and correlation (XC) potential was described by the Perdew–Burke–Ernzerhof (PBE) form within the generalized gradient approximation (GGA) [44]. For the Brillouin Zone integration, Gamma point was used. The kinetic energy cutoff for the plane-wave basis set was 360 eV. The total energies were minimized with an energy tolerance of 10^{−4} eV. All atomic positions and lattice constants were optimized with the conjugate gradient method.

Both FPMD and CMD simulations were performed at equilibrium. We used a (4 × 4 × 4) bcc-Fe supercell containing 432 atoms and substituted 64 randomly distributed Fe atoms by Zr atoms, corresponding to a Zr content of 14.81%, close to the target of 15%. As one of our aims is to do accurate electronic structure calculations using ab-initio density functional theory, we performed benchmark calculations to have a comparison between first principles and classical molecular dynamics simulations. A 432 atom cell was chosen to have the compromise between numerical accuracy and efficiency. We also showed the tested structure as a function of system size by using 6750 atoms.

The produced Fe_{0.85}Zr_{0.15} alloy was used to produce metallic glass with both FPMD and CMD simulations with the following heating and quenching procedure. First, the structure was heated to 5000 K for 1125 fs followed by the quenching to 2000 K with a 51.28 × 10¹⁴ K/s cooling rate. This fast quenching step is required to prevent clustering of Zr atoms. The structure was equilibrated at 2000 K for 135 fs. Thereafter, the structure was quenched to 300 K with a 49.71 × 10¹³ K/s cooling rate and further equilibrated at 300 K for 3420 fs. With FPMD, the temperature re-scaling was performed by resetting the temperature every 45 fs with 1 fs time step throughout the above production steps of the heating and quenching procedure. A reasonable cooling rate was chosen so that we can efficiently produce glass in first principles calculations while keeping the agreement with classical molecular dynamics approach. Specifically, the formation of a crystal is avoided by applying fast quenching from 5000 K to 2000 K.

With CMD, we used the *Berendsen Thermostat* [45], which rescales the velocities at every time step from v to λv where λ is given by

$$\lambda = 1 + \frac{\Delta t}{\tau} \left(\frac{T_0}{T} - 1 \right) \quad (1)$$

where T_0 equals the desired temperature, T is the system's actual temperature, Δt is the time window during which the system is adjusted to the desired temperature and τ is the temperature relaxation time. The ratio $\frac{\Delta t}{\tau}$ determines how rapidly the temperature is reset. Throughout all the above production steps with CMD, we used $\Delta t = 1$ fs and $\tau = 45$ fs.

Thermal conductivity, κ , was calculated employing the Green-Kubo(GK) theory of linear response, which is a standard approach to study heat and mass transport in amorphous systems [46,47]. GK method was used with classical molecular dynamics simulations in this paper. In this method, κ is obtained by integration of the auto-correlation function of the heat flux \mathbf{J} which is based on the fluctuation–dissipation theorem [48,49],

$$\kappa = \frac{V}{3k_B T^2} \int_0^\infty dt \langle \mathbf{J}(t) \cdot \mathbf{J}(0) \rangle \quad (2)$$

where V is the system volume, k_B is the Boltzmann constant, T is the temperature and the angular brackets denote an autocorrelation function. Numerically this implies the following calculation [50]:

$$\kappa = \frac{V}{3k_B T^2} \Delta t \sum_{m=1}^M \frac{1}{N-m} \sum_{n=1}^{N-m} \mathbf{J}(n+m) \cdot \mathbf{J}(n) \quad (3)$$

The total simulation time N was 2 ns. Every time step was used as time-origin and the difference between two time steps was set to $\Delta t = 1$ fs. Index n runs over the time-origins whereas index m runs over the time-lags. The maximum time-lag M was set to $M = 1000$ fs.

The heat flux \mathbf{J} is defined as

$$\mathbf{J} = \frac{1}{V} \left[\sum_i \epsilon_i \mathbf{v}_i + \sum_{i < j} (\mathbf{F}_{ij} \cdot \mathbf{v}_i) \mathbf{r}_{ij} \right] \quad (4)$$

where ϵ_i is the kinetic and potential energy of atom i , \mathbf{v}_i is the velocity of atom i , \mathbf{F}_{ij} is the force on atom i from atom j and \mathbf{r}_{ij} is the position vector of atom i relative to atom j . The first term describes the contribution of convection (diffusion of atoms) whereas the second term describes the energy transfer between neighboring atoms [46]. The atoms in our MD simulation do not diffuse and therefore the convection term is zero.

The calculation of thermal conductivity involves the position vector of every atom (Eq. (4)). But a unique definition of the position vector \mathbf{r} of the atoms in a periodic system is difficult. For CMD this was solved by Thomson et al. [51]. For FPMD, where the functionals depend on the electron density instead of the particle's energy and position vector, there are additional challenges. There are solutions to use GK method within FPMD method [46], but we use here GK only with CMD. MD simulations contain the information of normal, Umklapp and higher order phonon–phonon scattering through the dynamics of the

thermodynamic state of the system [47] but CMD has difficulties with treating the anharmonic interactions accurately [46].

We applied an *NVT* ensemble in CMD simulations until the potential energy reached a value within $10^{-4}\%$ of the desired potential energy, which was used as a convergence criterion [52], followed by an *NVE* ensemble simulation for 2 ns.

Metallic glasses with nanostructured voids (MGNV) were generated by creating periodic spherical voids in MG samples. First, MGNV were equilibrated at 300 K (*NVT*-CMD) using the *Berendsen Thermostat* to decrease temperature oscillations. The following procedure was used to couple the MGNV to a heat bath where the relaxation time τ was increased in each step (see Eq. (1)). τ was set as 1 fs for the first 100 ps. $\tau = 5$ fs was used for the next 200 ps followed by $\tau = 10$ fs for a time period of 300 ps. Finally, $\tau = 1$ ps was used for 1 ns time. Finally, κ (Eq. (2)) was calculated based on a 2 ns *NVE*-CMD simulation.

To calculate the vibrational density of states (VDOS) $g(\omega)$, Fourier transform of the velocity auto-correlation function $v_i(t)$ was performed (Eq. (5))

$$g(\omega) = \frac{1}{3N K_B T} \int_{-\infty}^{\infty} dt \sum_i \langle \mathbf{v}_i(t + \tau) \cdot \mathbf{v}_i(\tau) \rangle e^{i\omega t} \quad (5)$$

where i denotes the i th atom, τ is the time origin and N is the total number of the atoms in the unit cell. A set of 100 configurations taken at intervals of 25 ps was used to perform a converged VDOS. VDOS includes all possible excitations in the system. However, the contribution of each excited mode can be found by calculating the participation ratio (PR), which is given in (Eq. (6)) [53],

$$PR(\omega) = \frac{1}{N} \frac{(\sum_i g_i(\omega)^2)^2}{\sum_i g_i(\omega)^4}. \quad (6)$$

We also define shell-wise participation ratio where the shells are defined as confined volumes with two different diameters from the center of the simulation box. This participation ratio concerns only the atoms N_s contained in the respective confined volumes. This can be quantified as

$$PR_s(\omega) = \frac{1}{N_s} \frac{(\sum_i^{N_s} g_i(\omega)^2)^2}{\sum_i^{N_s} g_i(\omega)^4}. \quad (7)$$

In the crystalline case when PR is 1 according to Eq. (6), this corresponds to a phonon mode. However, in amorphous solids, there are extendons and locons. Extendons include both propagons and diffusons. Propagons are a kind of plane wave propagating modes like phonons. Although diffusons are propagating modes, they cannot be represented as plane waves. On the contrary, the locons can be imagined as localized modes confined at the atomic region without propagation. Until the Ioffe–Regel limit, propagons are the dominant vibrational modes. Between Ioffe–Regel limit and mobility edge, the vibrational modes are mostly contributed by the diffusons. Beyond the mobility edge, locons are the dominant excitations. The decreasing value from “1” in PR with increasing frequency shows the fingerprints of *propagons*, *diffusions* and *locons* in an amorphous system. Here, we aim to investigate the effects of voids on thermal conductivity [54,55] and hence, the difference between the systems with and without voids is a relevant quantity. We quantified the increase/decrease with respect to the bulk by dividing to the bulk as expressed in the equation below.

$$\Delta g(\omega) = \frac{g_0(\omega) - g_v(\omega)}{g_0(\omega)}. \quad (8)$$

$$\Delta PR(\omega) = \frac{PR_0(\omega) - PR_v(\omega)}{PR_0(\omega)} \quad (9)$$

where v represents the system with voids and 0 refers to the pristine system with 432 atoms.

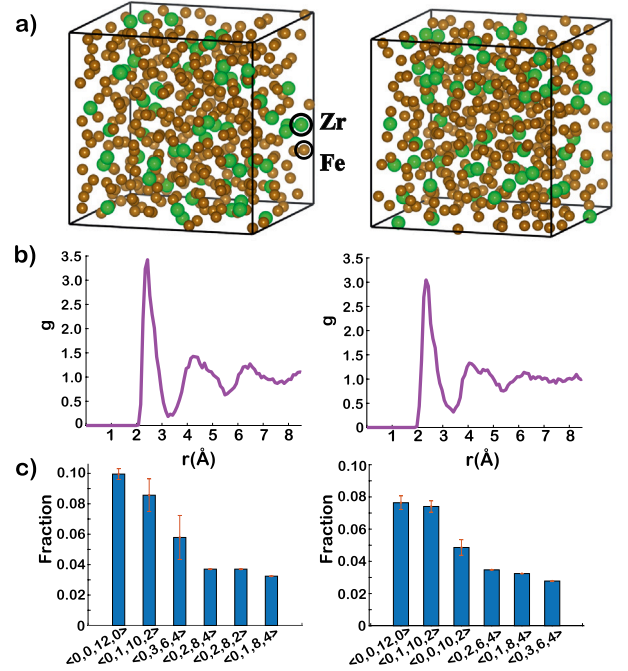


Fig. 1. (a) Simulated structural configurations of $\text{Fe}_{0.85}\text{Zr}_{0.15}$ metallic glasses by using Classical Molecular Dynamics (CMD) (left) and First Principles Molecular Dynamics (FPMD) (right). Brown balls and green balls are, respectively, Fe and Zr atoms. (b) Radial distribution function (RDF) of the glass produced by using CMD (left) and FPMD (right) after the final equilibration at 300 K. (c) Voronoi tessellations of the final glass structures produced with CMD (left) and FPMD (right).

2. Results and discussion

2.1. Structural analysis of MG

For the following structural analysis of the metallic glass we compare glass structures obtained with CMD and FPMD for the same volume V_{FPMD} of $\text{Fe}_{0.85}\text{Zr}_{0.15}$ at 300 K. The volume V_{FPMD} corresponds to the FPMD-calculated equilibrium structure of $\text{Fe}_{0.85}\text{Zr}_{0.15}$. In Fig. 1(a) we show the calculated atomic distribution within the unit cell at 300 K. The unit cell has a dimension of $a_{FPMD} = 17.30$ Å in all three directions.

In Fig. 1(b), we show the calculated radial distribution function (RDF) after the final equilibration at 300 K obtained from CMD (left) and FPMD (right) simulations. The bin size was set to 0.09 Å. The last four atomic configurations 45 fs apart from each other were used to obtain the RDF at the end of the equilibration production step. Both RDF plots show the expected decrease of the long range order and the splitting of the second peak, which is a characteristic property of a random closed packed structure, i.e. a metallic glass [56]. A Gaussian fit to the first RDF peak gives a nearest neighbor distance of 2.33 Å which agrees with the calculated Fe–Fe nearest neighbor distance. The RDF analysis of only Fe–Zr distances yields a Fe–Zr nearest neighbor distance of 2.67 Å.

The use of V_{FPMD} during the glass creation, independent of the MD method, implies that the FPMD quenching produced MG structure (right panel, Fig. 1b) is obtained for zero external pressure, whereas the CMD quenching produced MG structure (left panel, Fig. 1b) is obtained under an external pressure of close to 100 kbar. Comparing the FPMD and CMD produced MGs, the FPMD is slightly superior regarding both the absence of long-range order and presence of the splitting of the second peak.

In Fig. 1(c), we show the calculated Voronoi tessellations for the structures obtained from CMD (left) and FPMD (right) simulations. The

Table 1

Structural composition and thermal conductivity of MGNV, which were tailored from the $\text{Fe}_{0.85}\text{Zr}_{0.15}$ metallic glass (MG) unit cell (within the periodic boundary conditions) by removing a varying number of atoms thereby creating central spherical voids with varying diameters defined in units of the lattice constant a_{CMD} (first column) and the total number of remaining atoms (N_0) (second column). In columns three (N_{Fe}/N_0) and four (N_{Zr}/N_0), the glass composition of the MGNV is listed with Fe atoms (N_{Fe}) and Zr atoms (N_{Zr}). In column five we list the porosity $b = \frac{n}{N_0}$, i.e. the ratio of the extracted number of atoms from the cell (n) to the total number of atoms in the MG without void inside ($N_0 = 432$). In column six, the calculated thermal conductivities including their uncertainties are listed.

Sphere diameter (a_{CMD})	N_0	Fe %	Zr %	b	κ_{GK} (W/m K)
0	432	85.19	14.81	0	1.27 ± 0.10
0.25	428	85.28	14.72	0.01	1.20 ± 0.09
0.4	419	84.96	15.04	0.03	1.11 ± 0.10
0.5	405	85.19	14.81	0.06	0.97 ± 0.08
0.6	388	85.31	14.69	0.10	0.96 ± 0.08
0.75	338	85.21	14.79	0.22	0.71 ± 0.08
0.8	318	84.91	15.09	0.26	0.72 ± 0.07
1.0	206	83.01	16.99	0.52	0.28 ± 0.04

Voronoi tessellation with the highest fraction (10% in CMD, almost 8% in FPMD) corresponds to the ideal icosahedron, $\langle 0, 0, 12, 0 \rangle$, with a (geometrical) coordination number of 12 [57]. The next highest fraction has the $\langle 0, 1, 10, 2 \rangle$ Voronoi tessellation which is a typical icosahedral-like tessellation with one more added neighbor atom [58]. For Fe atoms, we find on average between 12 to 13 geometrical neighbors whereas for Zr-atoms, we find between 15 to 16 geometrical neighbors. This agrees with earlier findings where the free volume associated with Zr was found to be larger than for the 3d atom [59].

The calculated fractions of Voronoi tessellations differ slightly between CMD and FPMD, where we obtain with CMD a higher fraction of $\langle 0, 0, 12, 0 \rangle$ tessellations. Wang et al. [57] have shown a strong dependence of the occurrence of icosahedral like Voronoi tessellations and the atomic density where the occurrence of the $\langle 0, 0, 12, 0 \rangle$ is maximal for the random closed packed structure with a filling factor of 0.637. The calculated equilibrium lattice constant of $(\text{Fe}_{0.85}\text{Zr}_{0.15})$ is for CMD 5% larger than for FPMD: $a_{\text{FPMD}} = 17.30 \text{ \AA}$ and $a_{\text{CMD}} = 17.58 \text{ \AA}$. In CMD simulations, the EAM pairwise potential gives rise to an atomic sphere radius of Fe (and Zr) that is larger than the same radius calculated with FPMD. Using V_{FPMD} in our CMD-calculations therefore gives a higher filling factor. It then follows that for CMD we calculate the Voronoi tessellations distribution to be more centered at the $\langle 0, 0, 12, 0 \rangle$ tessellation in agreement with the findings of Wang et al. [57]

2.2. Stability of voids

MGNV were obtained by creating spherical voids by removing atoms within a shell of radius R_{void} around the center of the cell, after the bulk system's volume was relaxed. In Table 1 we list the created spherical voids. In column 1 we list the spherical void diameter ($2R_{\text{void}}$) followed by the total number of atoms within the cell in column 2. In column 3 and 4 we list the atom percentage of Fe and Zr within the cell. We checked whether the produced MGNV were still metallic by performing a PBE-VASP calculation of the electronic structure based on the geometries produced at the end of the 2 ns NVE simulation.

To analyze the voids' stability, we performed NVT simulations at constant temperature of 300 K. We find that the stability of the voids depends on the size of the void. Thus, the two smallest voids, i.e. $2R_{\text{void}} = 0.25a$ and $2R_{\text{void}} = 0.4a$, corresponding to 1% and 3% of atoms removed, respectively, are found to be unstable. In addition, all the stable voids change their shape from spherical to prolate ellipsoidal but they are clearly existent after 1.6 ns of MD simulation as is shown in Fig. 2.

To illustrate the void dynamics (and its collapse when occurring) during the CMD simulations, we show in Fig. 2 the initial and final

atomic positions for different MGNV. For the sake of clarity and to better illustrate the void dynamics, we only show a slice of the computational cell. In each panel that represents a distinct void size, we show at the top of the panel the initial atomic positions ($t = 0$) and at the bottom, the atomic positions at the end of the MD simulations ($t = 1.6 \text{ ns}$). The left side of each panel depicts a single unit cell, while the right side shows the 3×3 periodically repeated unit cell. For the void diameter 1.0, we also show in the middle, a plot of the full cell to emphasize the network of atomic bonds. As discussed above, only the larger void sizes (0.5, 0.6, 0.75, 0.8 and 1.0) remain stable after $t = 1.6 \text{ ns}$. During the 1.6 ns MD simulation the atoms in the MGNV do not diffuse but vibrate around their equilibrium position. For a void of size $R_{\text{void}} = 0.25$ ($R_{\text{void}} = 0.4$) 4 atoms (13 atoms) were extracted. Thus a void, where a cluster of 13 atoms or less is removed, is filled up by the remaining metallic glass network and the structure is self-healed. On the other hand, voids, where a cluster of 27 atoms or more is removed, are stable.

Now we discuss the relative position of an atom with respect to the center of the cell. The atomic positions are extracted from the MD trajectories and collected in bins of width $(a_{\text{CMD}} - R_{\text{void}})/10$. In Fig. 3, we show histograms of the distance, where the distance is integrated over all atoms. On the y-axis we plot the number of atoms that during the given time window have a distance within the given bin width (raw counts) divided by the total number of raw counts of all stacked histograms and the bin width such that the area of the sum of the histograms in each panel is normalized to one.

The width of the time window is increasing along the MD trajectory, such that the histogram corresponding to the final time window (blue) is a factor 100 larger than for the starting time window (yellow). The dashed gray line marks the void radius at $t = 0$. Our cell has a lattice constant of $a_{\text{CMD}} = 17.58 \text{ \AA}$. Along a lattice vector the largest possible distance from the center of the cell is 8.79 \AA , along the face-diagonal $\sqrt{2} \cdot 8.79 = 12.43 \text{ \AA}$ and along the space-diagonal the largest possible distance from the center is $\sqrt{3} \cdot 8.79 = 15.22 \text{ \AA}$.

For example, in the histograms for $2R_{\text{void}} = 0.75 \cdot a_{\text{CMD}}$ the dashed line is at $R_{\text{void}} = 6.59 \text{ \AA}$. At $t=0$, zero atoms have a distance to the center smaller than R_{void} . But already within the first time window, 0–50 ps, we find counts in the histogram for distances between 5 \AA up to R_{void} . This indicates that some atoms have moved towards the center of the cell whereby the shape and size of the void is altered. This explains the occurrence of counts to the left of the dashed line. The time evolution of the histograms reveals that the void with $R_{\text{void}} = 0.75 \cdot a_{\text{CMD}}$ is unaltered after the initial relaxation which occurs already within the first 10 ps.

A deeper analysis of the MD trajectories reveals that the sphere has become an ellipsoid with the following radii in the three orthogonal directions: 6.69 \AA , 6.55 \AA , 6.64 \AA . In two directions, the void diameter has increased (+1.5%, +0.08%), and in one direction it has decreased (−0.06%). For $2R_{\text{void}} = 0.8 \cdot a$ and $2R_{\text{void}} = 1.0 \cdot a$ we find a similar ellipsoid but with increasing asymmetry: For $2R_{\text{void}} = 0.8 \cdot a$ (+4.4%, +0.04%, −1.3%) and for $2R_{\text{void}} = 1.0 \cdot a$ (+5.8%, +1.0%, −2%). We conclude that for the three largest voids, the remaining atoms undergo a non cubic relaxation and compactify (i.e. the void has expanded). For the smaller voids, we find a different pattern: For $2R_{\text{void}} = 0.6 \cdot a$ (−13%, −13%, −11%), for $2R_{\text{void}} = 0.5 \cdot a$ (−19%, −6%, −5%). In contrast to the three largest voids, for the two smaller and stable voids, the remaining atoms instead prefer an increased space (i.e. the void is instead contracted).

As a reference, we also show the histograms of atomic distances for the MG without void ($R_{\text{void}} = 0$). In the MG without void, we constructed our supercell such that no atom is present at the center. However, it is found that for $R_{\text{void}} = 0.25 \cdot a_{\text{CMD}}$ one atom gets closer to the center than in the MG without void already during the first 0–50 ps. A deeper analysis of the MD trajectories shows that this happens within the first 1.4 ps. Moreover, we conclude from the different histograms that the atoms do not diffuse but only vibrate around their equilibrium positions because the shape of the histograms is maintained as a function of time, i.e. the histograms are self-similar.

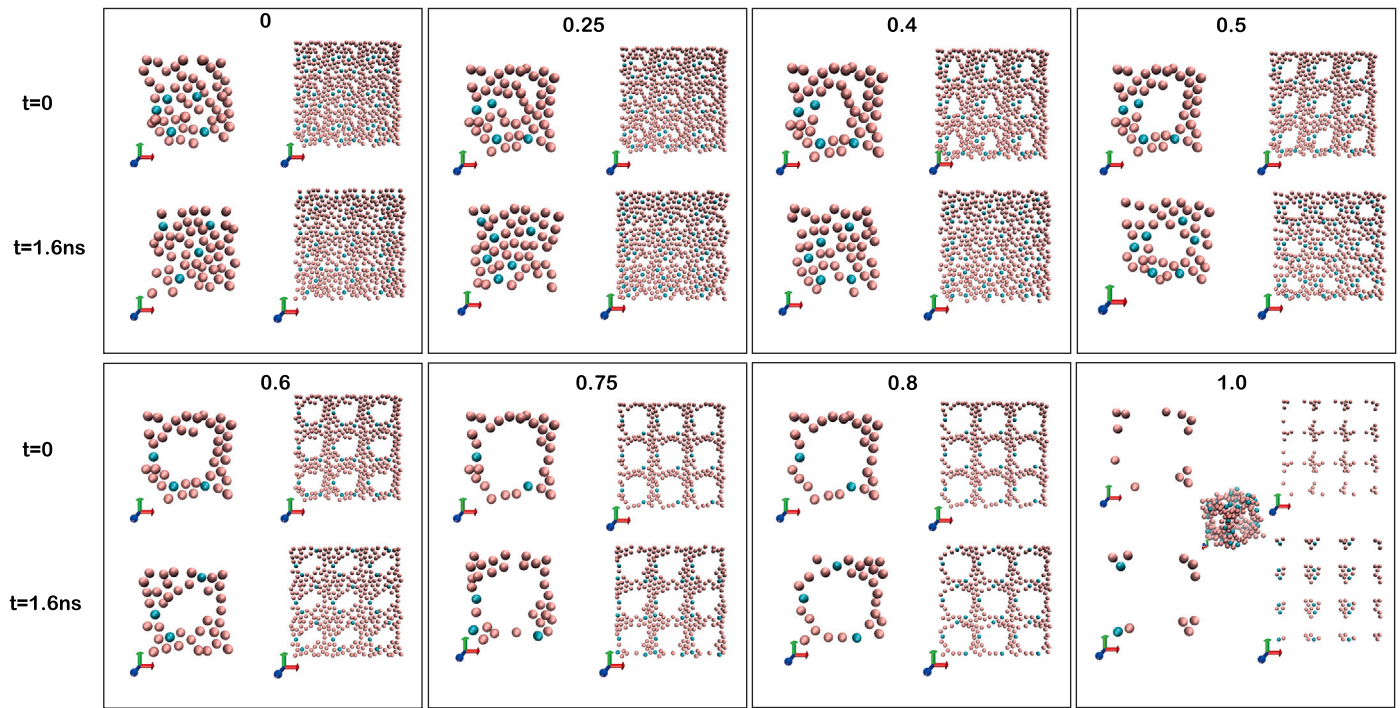


Fig. 2. Slices of 2 \AA thickness of the MGNV for varying void diameters calculated with (NVT)-CMD. For every void size we show in the top panel the starting configuration ($t = 0$), in the bottom panel the atomic positions within the same slice after $t = 1.6 \text{ ns}$, to the left the slice of the unit cell and to the right the slice of the 3×3 periodically repeated unit cell. For the void diameter 1.0 we also show in the middle a plot of the full cell to emphasize that the void structure is still connected.

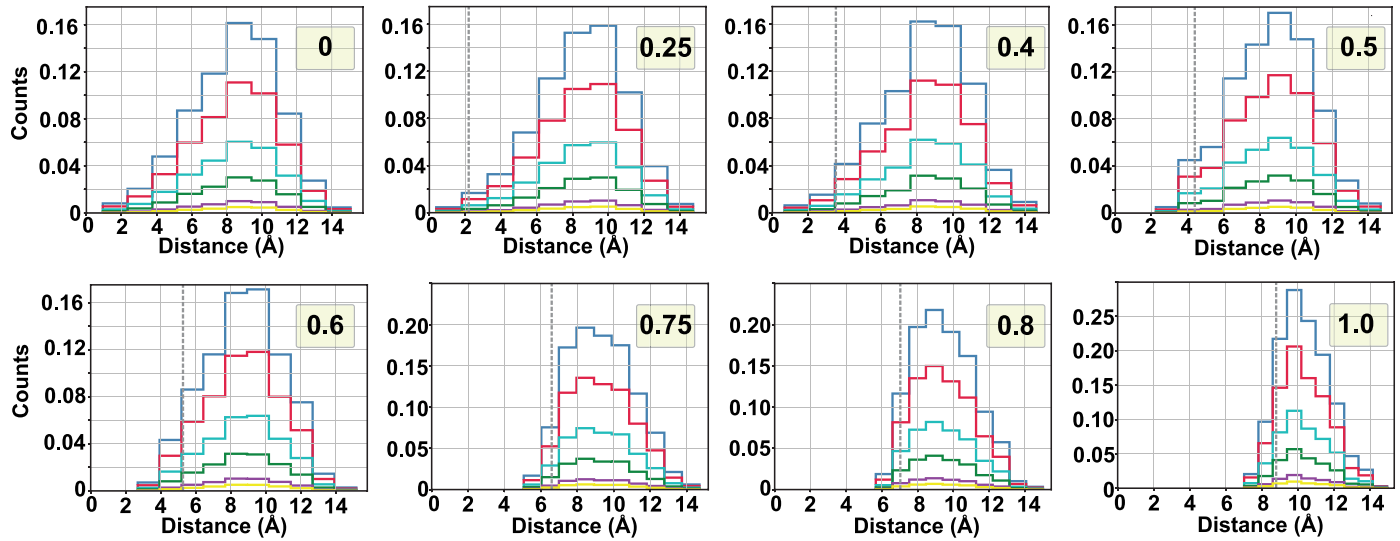


Fig. 3. Histograms of atomic distance integrated over all atoms and over a time window of the MD trajectory: 0–50 ps (yellow), 50–100 ps (magenta), 100–300 ps (green), 300–600 ps (cyan), 600–1100 ps (red), 1100–1600 ps (blue) and the dashed gray line (void radius) are shown for each MGNV with void diameter (in units of a_{CMD}) 0, 0.25, 0.4, 0.5, 0.6, 0.75, 0.8 and 1.0 as marked on the plots.

2.3. Lattice thermal conductivity

In the following, we present calculations of the lattice thermal conductivity using the Green-Kubo method (Eq. (2)). For simplicity, we refer in the following to thermal conductivity implying only its lattice contribution. Before computing the thermal conductivity, we followed the same thermal equilibration steps (NVT-CMD) as defined in the methods section. We calculate $\kappa = 1.27 \pm 0.10$ (W/m K) with CMD employing the FPMD quenching produced MG structure with the LAMMPS equilibrium lattice constant of $\text{Fe}_{0.85}\text{Zr}_{0.15}$ ($a_{CMD} = 17.58 \text{ \AA}$). We obtain the same κ for both the CMD quenching produced

MG structure, $MG(CMD)$ and the FPMD quenching produced MG structure, $MG(FPMD)$.

In Fig. 4(a) and (b), we show the time evolution of the heat flux and the convergence of κ on time averaging. The heat flux (Fig. 4,a) fluctuates around zero as expected in an equilibrium MD simulation and κ becomes stable within reasonable error bars after a time averaging over about 1000 ps (Fig. 4,b).

2.4. System size dependence

We made a comparison of the system's size effect on the calculated thermal conductivity by increasing the system's size 2.5 times by

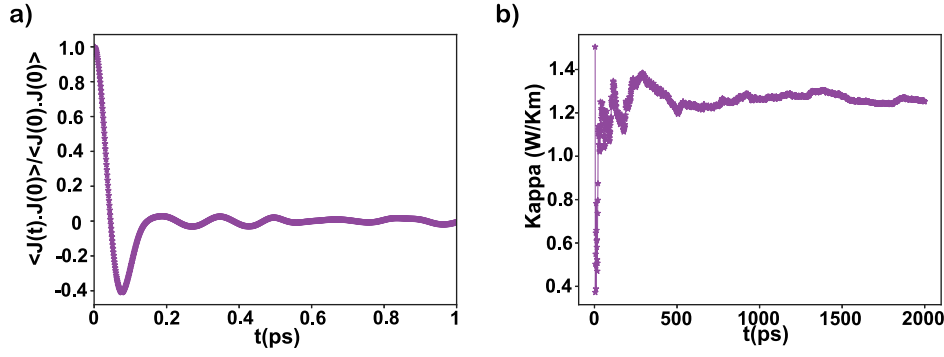


Fig. 4. Time convergence of thermal conductivity, κ , of $\text{Fe}_{0.85}\text{Zr}_{0.15}$ metallic glass (MG): (a) Time dependence of heat current autocorrelation function and (b) thermal conductivity as a function of the simulation runtime of 2 ns (NVE)-MD.

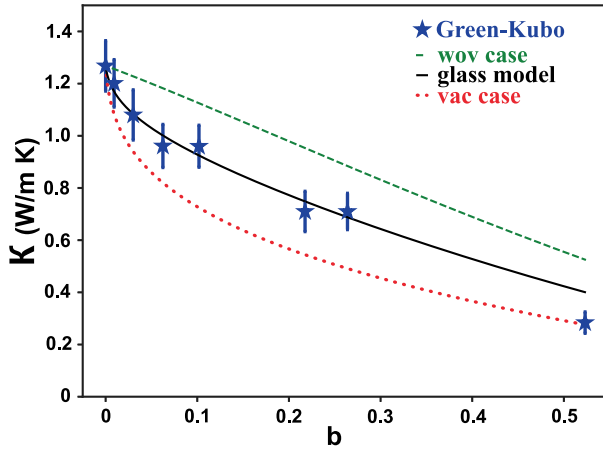


Fig. 5. Thermal conductivity calculated with Green-Kubo (Eq. (2)) (blue) as a function of the voids of the MGNV, $b = n/N_0$, where n is the number of extracted atoms creating the starting void and N_0 is the number of atoms in the MG without void. Vertical bars correspond to uncertainty. The solid line corresponds to the glass model (Eq. (13)), the dashed line shows one of the limits; without voids (*wov*) (Eq. (11)) and the dotted line shows the other limit; vacuum continuous (*vac*) (Eq. (12)).

Table 2

Comparison of large and relatively smaller cell's thermal conductivity values with NVT and NPT ensembles by keeping constant $\sim 85\%$ Fe and $\sim 15\%$ Zr at 300 K.

Ensemble	Density ($\text{u}/\text{\AA}^3$)	Volume (\AA^3)	N	κ (W/m K)
NVT	4.86	5435.13	432	1.26 ± 0.08
NVT	4.86	84 923.89	6750	1.26 ± 0.08
NPT	~ 4.84	85198.23 ± 11.45	6750	1.27 ± 0.08

keeping constant the density and following the steps defined in the production and MD procedures. The results showed that the system's size has an insignificant effect on thermal conductivity. We made further analysis of our obtained small system by comparing it with the thermal conductivity of the larger system which is calculated with NPT to continue with small system size. All the analyses support that the thermal conductivity can be calculated reliably with the obtained volume including 432 atoms, as can be seen in Table 2.

In Fig. 5, we show the calculated κ of the MGNV as a function of the porosities $b = n/N_0$, i.e. as a function of the ratio between the number of extracted atoms, n , and the number of total atoms in the original MG, N_0 . We define the void parameter b as,

$$b = \frac{n}{N_0}. \quad (10)$$

The blue stars in Fig. 5 correspond to the calculated κ , also listed in Table 1. The vertical line across each star corresponds to the uncertainty in κ . It is defined as the standard error ($\kappa/\sqrt{N_0}$, where N_0 is the

number of atoms in the cell) and is caused by the temperature fluctuation during the MD simulation. The dashed and dotted lines correspond to the model, which was inspired from Russell's model [60,61]. The solid line is the weighted linear combination of the two limiting cases and is termed the 'glass model'.

The first limiting case is without void (*wov*), where the atoms are packed with vacuum in between them (*wov* case) and the second limit is the vacuum continuous (*vac*), where none of the atoms exists (*ac* case).

For the *wov* case κ_{wov} as a function of porosity $b = n/N_0$:

$$\kappa_{wov}(b) = \kappa_0 \frac{b^{\frac{2}{3}} + \frac{\kappa_0}{\kappa_V} (1 - b^{\frac{2}{3}})}{b^{\frac{2}{3}} - b + \frac{\kappa_0}{\kappa_V} (1 - b^{\frac{2}{3}} + b)} \quad (11)$$

where $\kappa_V = 0.0$ (W/m K) is the thermal conductivity of vacuum. κ_0 is a scaling factor and is equal to the calculated κ of the $\text{Fe}_{0.85}\text{Zr}_{0.15}$ MG. The *wov* case is shown as the green dashed line in Fig. 5. κ decreases linearly with void parameter or, in other words, with decreasing density of the void including system, the conductivity is decreasing.

For the *vac* case model κ_{vac} :

$$\kappa_{vac}(b) = \kappa_0 \frac{b^{\frac{2}{3}} - b + \frac{\kappa_V}{\kappa_0} (1 - b^{\frac{2}{3}} + b)}{b^{\frac{2}{3}} + \frac{\kappa_V}{\kappa_0} (1 - b^{\frac{2}{3}})} \quad (12)$$

The *vac* case of the model is shown as the red dotted line in Fig. 5. For small voids, κ_{vac} shows a steep linear decrease which then flattens out. Here, in contrast to the *wov* case, vacuum and without void structures are interchanged. As Russel pointed out, this is unstable, but we can assume that the structures is connected at corners or at a limited number of points. The model predicts for both cases (*wov* and *vac*) the limiting behavior correctly, i.e. $\kappa_{wov} = \kappa_{vac} = \kappa_0$ in the limit of $b = 0$ and $\kappa_{vac} = \kappa_{wov} = \kappa_V$ in the limit of $b = 1$. We want to emphasize that the model does not contain any fitting parameter.

The two cases (*wov* and *vac*) of the model determine the range in which we expect thermal conductivities to fall: For a given void size, a material cannot have a lower thermal conductivity than the vacuum model because this lower bound implies a situation where the material is in vacuum, i.e. the number of conduction pathways through the material is minimal. On the other hand, for a given porosity, a material cannot have a higher thermal conductivity than the voidless model because this higher bound implies a situation where the vacuum is immersed in the system, i.e., the number of conduction pathways through the material is a maximum. In agreement with this interpretation, all of our calculated κ values lie within the range determined by the two limiting cases of the models. In Fig. 5 this is seen by noticing that all blue stars (calculated κ values) lie in between the dashed and dotted lines.

In addition, the calculated κ (blue stars in Fig. 5) is best described by a linear combination of the solid continuous (*wov*) and air continuous (*vac*) cases:

$$\kappa(b) = \frac{1}{2}(\kappa_{wov} + \kappa_{vac}) \quad (13)$$

Table 3

Thermal conductivity of $\text{Fe}_{0.85}\text{Zr}_{0.15}$ metallic glasses (MGs) which were calculated by using CMD with Green-Kubo (GK) method. MG_{test} and $\text{MGNV}_{\text{test}}$ share the same volume ($V = 5443 \text{ \AA}^3$) and porosity but differ in the existence of a void. κ of $\text{MGNV}_{\text{test}}$ is repeated here from Table 2 for convenience.

	κ (W/m K)	
	MG_{test} (no void)	PG_{test} (with void)
$b = 0.06$	0.89 ± 0.08	0.96 ± 0.08
$b = 0.10$	0.91 ± 0.08	0.89 ± 0.08

which is shown as the black solid line in Fig. 5. We term this last model the ‘glass model’.

This glass model predicts the dependence of the thermal conductivity on porosity rather good. In agreement with expectations, κ decreases with increasing void size (Table 1), i.e. increasing porosity (Fig. 5). The calculated κ with the highest porosity ($b = 0.52$) agrees better with the *vac* case of the Brick model. From Fig. 2 we see that the structure with the highest porosity (void diameter 1.0) is indeed disconnected along the shown slice in contrast to the other voids. We want to emphasize that the structure is still connected along the frame, the MG not being stable otherwise.

If we interpret the two cases (*wov* and *vac*) in terms of pathways through the material, we can state that in the *wov* case conduction is exclusively determined by pathways through the material. In other words, the higher the density, the more pathways exist. In contrast, in the *vac* case, conduction is mainly determined by the very few pathways still existing between the remaining material. Pathways through air are very few and in the limit of vacuum equal to zero. In an ordered material we will encounter much more pathways than in a disordered material. The inclusion of voids in a disordered material can therefore be viewed as a case in between *wov* and *vac* cases of the models.

Analyzing in terms of conduction pathways on an atomistic level, we realize that the disorder of our short range ordered atoms (icosahedra) can be viewed as if the icosahedra were immersed in vacuum. On the other hand, as long as icosahedra share more than just corners with other icosahedra, the conduction pathways in MGNV are less than in an ordered solid but more than in a *vac* case. Therefore we suggest a superposition of the *wov* and *vac* cases for MGNV. This superposition is the content of the glass model (Eq. (13)). The simplicity of the model leads us to believe that it is valid for a broad range of void including ordered and disordered materials.

Even for the two structures where the voids become unstable, we find a decrease in κ values. The effect of the void on κ is thus less dependent on the void-shape or the compactness of the additional free volume, but much more on the total number of possible pathways through the MGNV. A measure of the change of the possible pathways through the MGNV is envisioned in the porosity $b = n/N_0$. In order to test the independence of κ on the void-characteristics, we calculated κ for a MG, MG_{test} , with equal porosity and volume of MGNV but without a void.

The MG_{test} is produced by decreasing the volume of $\text{MGNV}_{\text{test}}$ such that the void disappears during a MD simulation. We then calculate κ for MG_{test} after having re-scaled the volume. In the MG_{test} the remaining ($N_0 - n$) atoms become more distributed more diluted such that the Fe-Fe nearest neighbor distance increases less (for $b = 0.06$ increase with 3%) than the first RDF peak position increases (for $b = 0.06$ increase with 11%).

This is explained by assuming that the free volume associated with the Zr atoms has increased more than the Fe-Fe bond-length becomes stretched. The calculated κ of MG_{test} for two different porosities is listed in Table 3 and lies within the two limiting cases of the Brick model. For porosity $b = 0.06$ ($b = 0.10$), the calculated κ for MG_{test} (without void) is 7% smaller (2% larger) than for $\text{MGNV}_{\text{test}}$ (with void). We conclude that in a MG the effect of the void on κ is not the void-shape or the compactness of the additional free volume, but much more the total

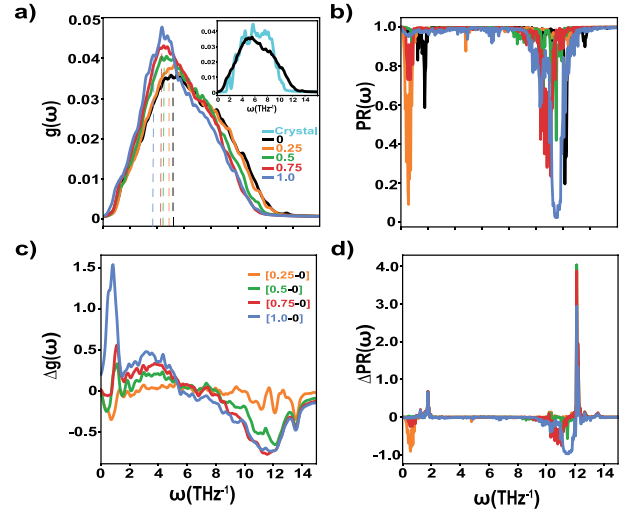


Fig. 6. (a) Calculated vibrational densities of states of 0; 0.25; 0.5; 0.75 and 1.0 voids. Dashed lines represent the position of the dominant peaks. (b) Participation ratio of the selected voids. (c) The selected voids' vibrational densities of states by subtracting the '0-VDOS' and dividing by '0-VDOS' to show a visible red shift with increasing void diameter. (d) The calculated PRs by subtracting the '0-PR' and dividing by '0-PR' to show the increasing localized modes with increasing void diameter.

number of possible pathways through the MG. We predict that in order to decrease the thermal conductivity in metallic glasses it is sufficient to remove material piece-wise while conserving the original volume.

3. Vibrational properties

The thermal conductivity of MGNV is directly affected by the number of atoms in the cell. Moreover, the decrease in thermal conductivity is related to the presence of the localized modes formed by the voids. Therefore, vibrational density of states $g(\omega)$, PR and ΔPR analysis are done for the four cases with the void diameters 0.25, 0.5, 0.75, and 1.0 times the lattice vector. $g(\omega)$ and $\Delta g(\omega)$ plots in Fig. 6 exhibit a red-shift with decreasing number of atoms in the cell and also an increase roughly until 7 THz followed by a decrease. The red-shift can be interpreted as the occurrence of more propagons and diffusions in the system relative to the pristine system as a result of broken bonds and modified heat transfer pathways, which is responsible for the decrease in thermal conductivity. The detailed analyses can be clearly seen in PR and ΔPR plots. The red-shift in $g(\omega)$ results from an increase in propagon, diffusion and locon modes. At a very low frequency, phonons and propagons are expected to exist. But the observed decrease of PR at low frequencies shows that the propagons become more dominant with increasing void diameter. At the range from 8 to 14 THz, locons become largely dominant. It remains to be investigated whether this red-shift and the presence of increasing locons are due of a contribution of diffusion-locon coupling. Large voids with diameters 0.75 and 1.0 show more distinct behavior in the increasing locon modes than the systems with smaller voids.

4. Temperature and pressure dependence of thermal conductivity

4.1. Absence of voids

Further analyses were done to understand if the thermal conductivity of the system under pressure and at different temperatures shows a different behavior with the increasing system size. The ambient pressure is denoted as *OP* with a volume of 5433.21 \AA^3 . The applied positive pressure (*PP*) value corresponded to $\sim 4.65\%$ shrink in the volume of the cell, whereas the negative pressure (*NP*) was equivalent to $\sim 1.72\%$ increase in the volume of the cell.

Table 4

Comparison of large and relatively smaller cell's thermal conductivity values with applied positive(PP), zero(OP) and negative(NP) pressures which are causing difference in the system's volume respectively ~4.65% decrease; no change; and ~1.72% decrease at 300 K.

System (N)	Pressure	Volume (\AA^3)	κ (W/m K)
432	PP	5180.45	1.41 ± 0.08
	OP	5435.13	1.26 ± 0.08
	NP	5526.46	1.13 ± 0.08
6750	PP	80 944.51	1.41 ± 0.08
	OP	84 923.89	1.26 ± 0.08
	NP	86 350.89	1.17 ± 0.08

Table 5

Comparison of thermal conductivities for two system sizes under zero(OP) at different temperatures respectively 200; 300; 500; and 700 K.

System (N)	Temperature	κ (W/m K)
432	200	1.19 ± 0.08
	300	1.26 ± 0.08
	500	1.28 ± 0.08
	700	1.26 ± 0.08
6750	200	1.21 ± 0.08
	300	1.26 ± 0.08
	500	1.26 ± 0.08
	700	1.29 ± 0.08

According to the results presented in Table 4, the system size does not have any significant effect on thermal conductivities. Both of the large and the small systems show the same decreasing behavior under negative pressure and increasing behavior under positive pressure. We also found that the systems' thermal conductivity explicitly has no temperature dependency. The small system's thermal conductivity got affected through the applied pressure and not affected through the temperature change (Tables 4 and 5). Therefore, we chose the small system to understand the effects in presence of the voids with varying pressure and temperature. The another reason to chose the system size smaller was to keep constant and same the system's density and void size under applied pressure, to be able to perform a reliable comparison. We also want to note that we did not include the low temperatures in the Table 5 as classical MD simulations need corrections which are caused by the quantum effects in the vibrational excitations at low temperatures [62]. The reason for not using NPT and sticking to only NVT calculations in this study was also to keep all the parameters constant except changing the pressure and temperature. This approach may be a good approximation to be used in today's and future's nano sized thermo-electrical device design methods and their simulations.

4.2. Presence of voids

The results presented in Table 6 show that the thermal conductivity of the pristine MG is sensitive to applied pressure and relatively less sensitive to varying temperatures. This is quite different for the systems with voids where a significant influence of temperature and pressure is observed. Therefore, it is possible to tailor thermal conductivity through the creation of nanostructured voids with different diameters. In addition, the already demonstrated idea of "The wider void diameter, the sharper decrease in thermal conductivity", we aimed to combine pressure and voids at the same time to fine-tune the thermal conductivity. We used the same void diameters and the defined three pressure values; PP, OP, and NP. The calculated values are presented in Table 6 and 1. At 300 K and under PP, all the structures show ~0.2 (W/K m) increase in their thermal conductivity, whereas under NP their thermal conductivity shows very small decrease for some structures; 0.5, 0.75, 1.0 due to less local structural changes supported by the analysis of calculated RDF. Therefore, one may conclude that the thermal conductivity can be tuned by creating voids and with

Table 6

Void size dependent thermal conductivities under different pressures: PP, OP, NP and at different temperatures.

Void diameter	Pressure	κ (W/m K)			
		200 K	300 K	500 K	700 K
Bulk	PP	1.41	1.41	1.33	1.38
	OP	1.19	1.26	1.28	1.26
	NP	1.19	1.15	1.18	1.21
0.25	PP	1.38	1.46	1.29	1.39
	OP	1.25	1.20	1.19	1.20
	NP	1.08	0.97	1.19	1.13
0.4	PP	1.27	1.28	1.26	1.29
	OP	1.24	1.11	1.11	1.17
	NP	1.0	1.12	1.13	1.16
0.5	PP	1.24	1.26	1.18	1.16
	OP	0.91	0.97	1.09	0.97
	NP	1.09	0.97	1.01	1.01
0.6	PP	1.33	1.12	1.00	1.03
	OP	0.90	0.96	0.95	0.94
	NP	0.78	0.91	0.93	0.92
0.75	PP	0.80	0.87	0.82	0.80
	OP	0.73	0.71	0.70	0.69
	NP	0.74	0.79	0.69	0.69
0.8	PP	0.51	0.79	0.70	0.72
	OP	0.74	0.72	0.65	0.68
	NP	0.69	0.63	0.64	0.62
1.0	PP	0.28	0.35	0.31	0.31
	OP	0.29	0.28	0.30	0.30
	NP	0.31	0.29	0.26	0.28

an applied external pressure to fine tune the thermal conductivity by roughly ± 10 –15% change.

We have also found that the thermal conductivity has no significant temperature dependence in the range of 200–700 K as shown in Table 7 and Fig. 7. This is particularly true for the case of OP. However, some variations can be observed at low temperatures for the cases of PP and NP for some structures where the void diameters are close to each other. These findings are supported by almost no change in RDF plots with varying temperatures. As a conclusion in this section, we have showed that the thermal conductivity can be tailored through voids and further $\pm \sim 10$ –15% tuning is possible through applied pressure, which can be explored in the development of thermoelectric materials.

5. Vibrational analysis

5.1. Absence of voids

In the previous section, we showed that the thermal conductivity has an insignificant dependence on temperature. This can be investigated in detail through the analysis of vibrational density of states (VDOS) and the corresponding participation ratio (PR). Firstly, our calculated VDOSs are *qualitatively similar* for two different system sizes as shown in the insets of Fig. 8. This is also true for the calculated PRs and the RDFs as shown in the figure. Therefore, we conclude that the smaller size can be used for further analysis of vibrational characteristics. As a further analysis, we also calculated mode participation ratio to obtain the contribution of specific atoms in heat transport. For this purpose, we selected the atoms situated in various spherical shells with increasing diameter from the center of the cell. It is important to note that the *extendons(propagons, diffusions) and localized modes* are the existing modes in a metallic glass [62]. The known limit between propagons and diffusions is the *Ioffe-Regel crossover frequency* where the propagons' wavelength becomes comparable to their mean free path. Beyond this limit, diffusions and localized modes with non-propagating nature become dominant. This transition frequency is the one where the *Boson Peak* is usually observed and is identified as

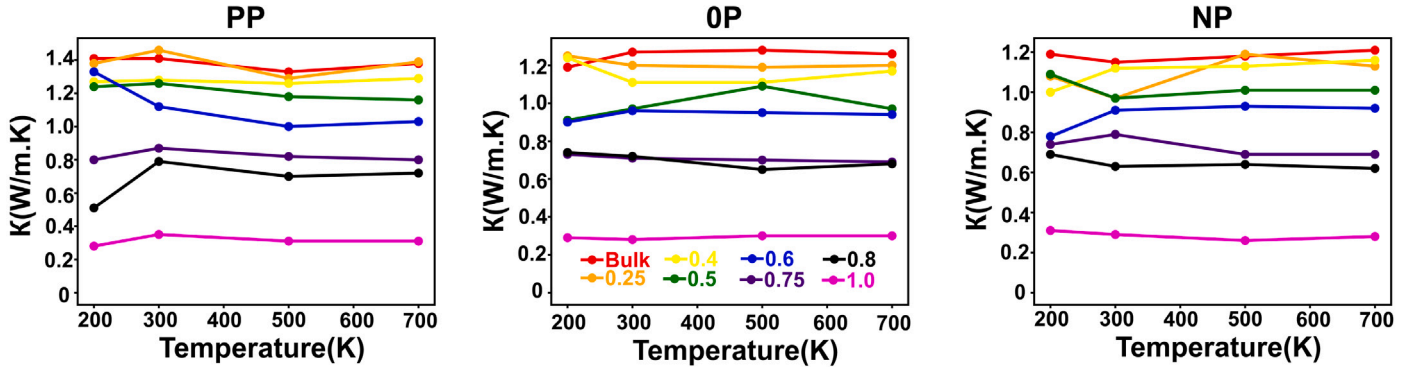


Fig. 7. Temperature dependence of thermal conductivity including voids under (a) 137 GPa (positive) pressure, (b) 0 pressure, (c) -5 kBar (negative) pressure.

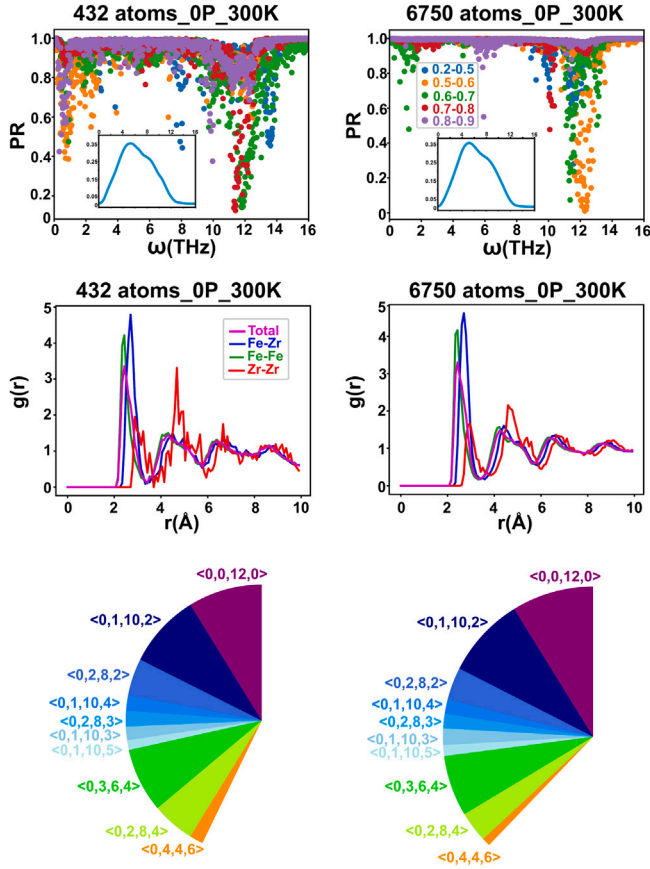


Fig. 8. At 300 K and under OP, the shell-wise participation ratios for two different system sizes are shown, along with an inset of the total vibrational density of states for both systems and the total and partial radial distribution functions. The distribution of Voronoi polyhedra for both systems is represented in the pie charts.

the transversal propagons' frequency. We have obtained this frequency around 1.40 THz by exploring a temperature range of 20–700 K. Even this peak changes with temperature and pressure, the kink at around 1.4 THz is always observed. This frequency was used to understand how the thermal conductivity is affected by the variation of temperature, pressure and voids. The studied frequency regions are marked as circles and triangles in Fig. 9. Another important point to note that these frequencies indicate the transition between diffusion and locon modes where the mobility edge changes and the diffusivity becomes zero in the infinite size limit. Although, a quantitative analysis of the modes is difficult without studying lattice dynamics, a qualitative interpretation of the locon modes can be done by PR. If the value of $PR(w) = 1$, all

Table 7

Comparison of large and relatively smaller cell's short range orderings fractions by using Voronoi tessellation method. CN and VP indicate coordination number and Voronoi polyhedra respectively.

System (N)	Types	CN	VP	Fraction
432	Full icosahedral	12	$\langle 0, 0, 12, 0 \rangle$	0.088
		13	$\langle 0, 1, 10, 2 \rangle$	0.088
		12	$\langle 0, 2, 8, 2 \rangle$	0.044
	Distorted icosahedral	15	$\langle 0, 1, 10, 4 \rangle$	0.019
		13	$\langle 0, 2, 8, 3 \rangle$	0.019
		14	$\langle 0, 1, 10, 3 \rangle$	0.016
		16	$\langle 0, 1, 10, 5 \rangle$	0.016
	Distorted BCC	14	$\langle 0, 3, 6, 4 \rangle$	0.076
	Distorted BCC	14	$\langle 0, 2, 8, 4 \rangle$	0.051
	Distorted FCC	14	$\langle 0, 4, 4, 6 \rangle$	0.016
6750	Full icosahedral	12	$\langle 0, 0, 12, 0 \rangle$	0.088
		13	$\langle 0, 1, 10, 2 \rangle$	0.087
		12	$\langle 0, 2, 8, 2 \rangle$	0.035
	Distorted icosahedral	14	$\langle 0, 1, 10, 3 \rangle$	0.018
		15	$\langle 0, 1, 10, 4 \rangle$	0.016
		13	$\langle 0, 2, 8, 3 \rangle$	0.015
		16	$\langle 0, 1, 10, 5 \rangle$	0.001
	Distorted BCC	14	$\langle 0, 3, 6, 4 \rangle$	0.067
	Distorted BCC	14	$\langle 0, 2, 8, 4 \rangle$	0.033
	Distorted FCC	14	$\langle 0, 4, 4, 6 \rangle$	0.001

atoms participate equally. If it is $\sim(1/N)$, one may interpret it as the onset of localized modes with the involvement of few atoms locally. Here, the value of PR should be less than 0.2 to identify this behavior.

Effects of confinement on the mode participation can be clearly seen for large systems. However, for our system size, we observe that the peak positions are in quite good agreement to a larger system size whereas the density of the mode participation changes. It is striking that this has no effect on thermal conductivity and local structural ordering from the point of view of Voronoi and RDF analyses. A detailed analysis of local structures is shown in Table 7 for two system sizes. Once again, the coordination numbers and the fraction of Voronoi polyhedra are quite similar for these two sizes.

According to the calculated participation ratio analysis on bulk structure in Fig. 9, we observed that the heat carriers' frequency was shifted and the localized modes decreased in all shells. Positive and negative pressures caused an increase localized modes at 200 K but not at 700 K. Positive pressure caused a slight blue shift in the modes' frequencies, while the negative pressure caused relatively higher blue shift in the modes' frequencies. In the insets of 9, temperature and pressure effects on the VDOS plots are represented better. With increasing temperature, slight changes in outer shells are visible even though participation ratio shows the mode type change sharper than VDOS for outer shells' heat carriers. Interestingly the changes are not causing an increase in thermal conductivity with increasing temperature. Meanwhile, pressure caused a more significant change on both VDOS and PR

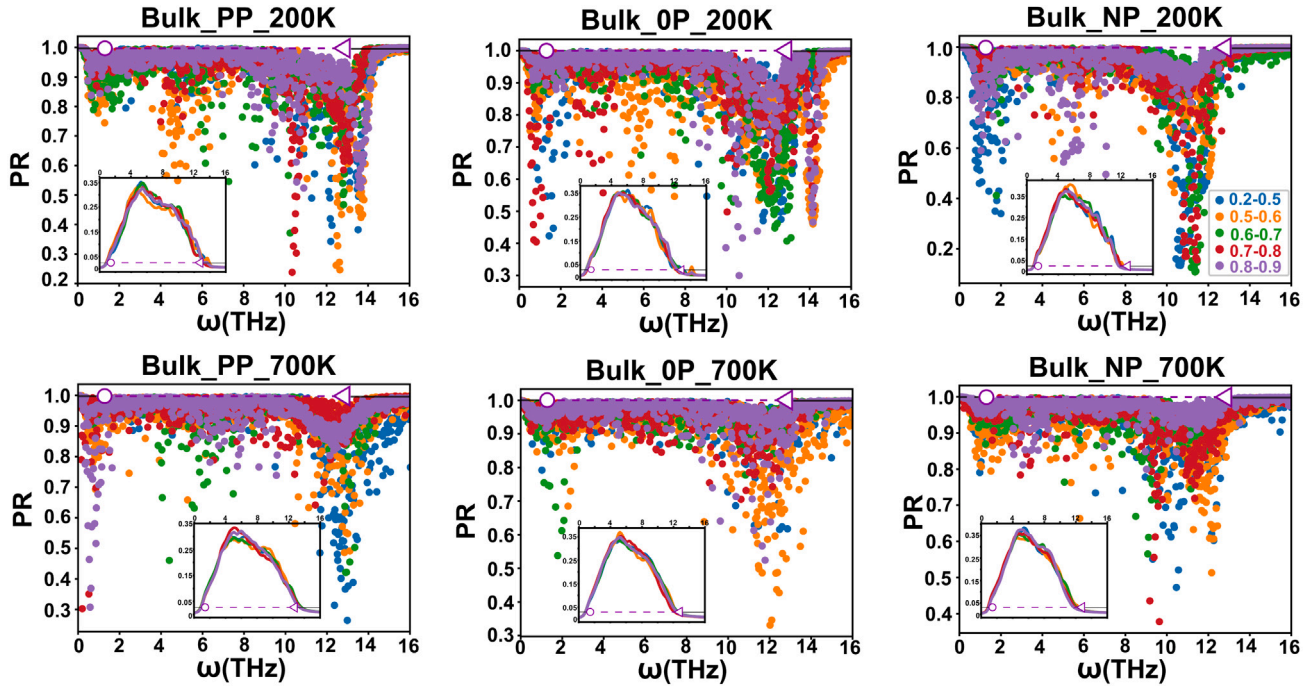


Fig. 9. Bulk system's shell-wise participation ratio at temperatures of 200 K and 700 K, and under applied pressures is shown. The insets represent the shell-wise vibrational densities of the system under the defined conditions.

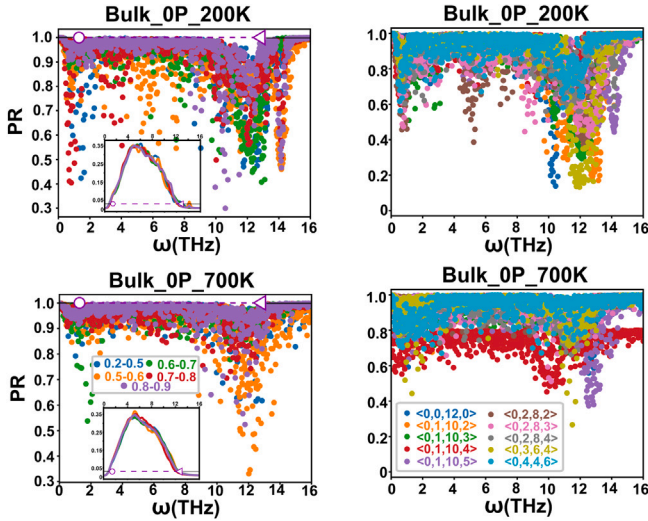


Fig. 10. The PR plots for the bulk system at 200 K and 700 K under OP are shown for the contributing atoms. On the left plots, the atoms which are located in the 0.2–0.5, 0.5–0.6, 0.6–0.7, 0.7–0.8, and 0.8–0.9 shells are shown. On the right plots, the atoms which are creating SROs: Full-Icosahedra, Distorted-Icosahedra, Distorted-BCC, and Distorted-FCC as defined in Table 7 are shown. The insets in the left plots show the vibrational density of states for the selected atoms in a shell-wise manner.

in shells. While PP can cause spreading in frequency in diffusion regime for all shells, NP accumulates creation of more peaks. This supports the idea of fine tuning of thermal conductivity with pressure.

The visible shift in frequency and sharp changes in outer shell's modes with pressure hint towards the effect of local structural ordering. Therefore, we focus on the atoms creating different SROs 10. The localized modes at around 10 to 12 Hz mainly arise from icosahedra, distorted Icosahedra and distorted bcc($\langle 0, 3, 6, 4 \rangle$) structures at 200 K where the localized modes are prominently visible. However, the dominance of localized modes fades away with increasing temperature. The

selected SROs are present mostly outside the 0.5 shell radius. As they contribute to non-propagating modes, a decrease in heat conductivity is observed.

5.2. Presence of voids

To show the voids' VDOS and PR, we selected 0.25, 0.5 and 0.75 diameter voids and used the shell definition defined above and further SROs analysis as shown in 11. As discussed in the above section, VDOS of the bulk structure at 200 K under PP showed increasing in localized mods and the more visible splitted second peak in VDOS. Therefore, to see a wider frequency range and local modes contribution, we selected to work at 200 K under PP. A clear effect of voids is a red-shift in the frequency regime. This shift increases the first peak intensity similar to the VDOS observed at NP with increasing void size from bulk to 0.75 void. While PR plots of shells' was showing a transition in heat carriers peak positions', a red-shift in VDOS frequencies of the 0.25 and 0.5 voids was occurring. The 0.25 voids' PR showed a participation to the localized modes from inner shell atoms instead of the outer shell's atoms in this case. This transition between atoms disappear with increasing void size. A reason for the observed transition can be related to reorientation of inner atoms relative to defect type void size. The PR showing SROs' contribution supports the idea of Distorted Icos and BCCs' contribution to localized modes as their density increases relative to bulk. It is strange and interesting 0.5 voids's outer shells give rise soft localized modes at 200 K which we do not expect to see at high temperatures actually. However this effect cannot be seen on SROs PR. But localized mode contribution from different SROs becomes increased with increasing size while full icosahedral contribution to localized modes becomes visible. In 0.75 void case perfect and distorted icosahedron density is increases because they are sitting outer shell mostly and their contribution to localized modes are also red-shifts.

6. Conclusions

We studied the structural properties of $\text{Fe}_{0.85}\text{Zr}_{0.15}$ metallic glass by molecular dynamics simulations at 300 K. The lattice thermal con-

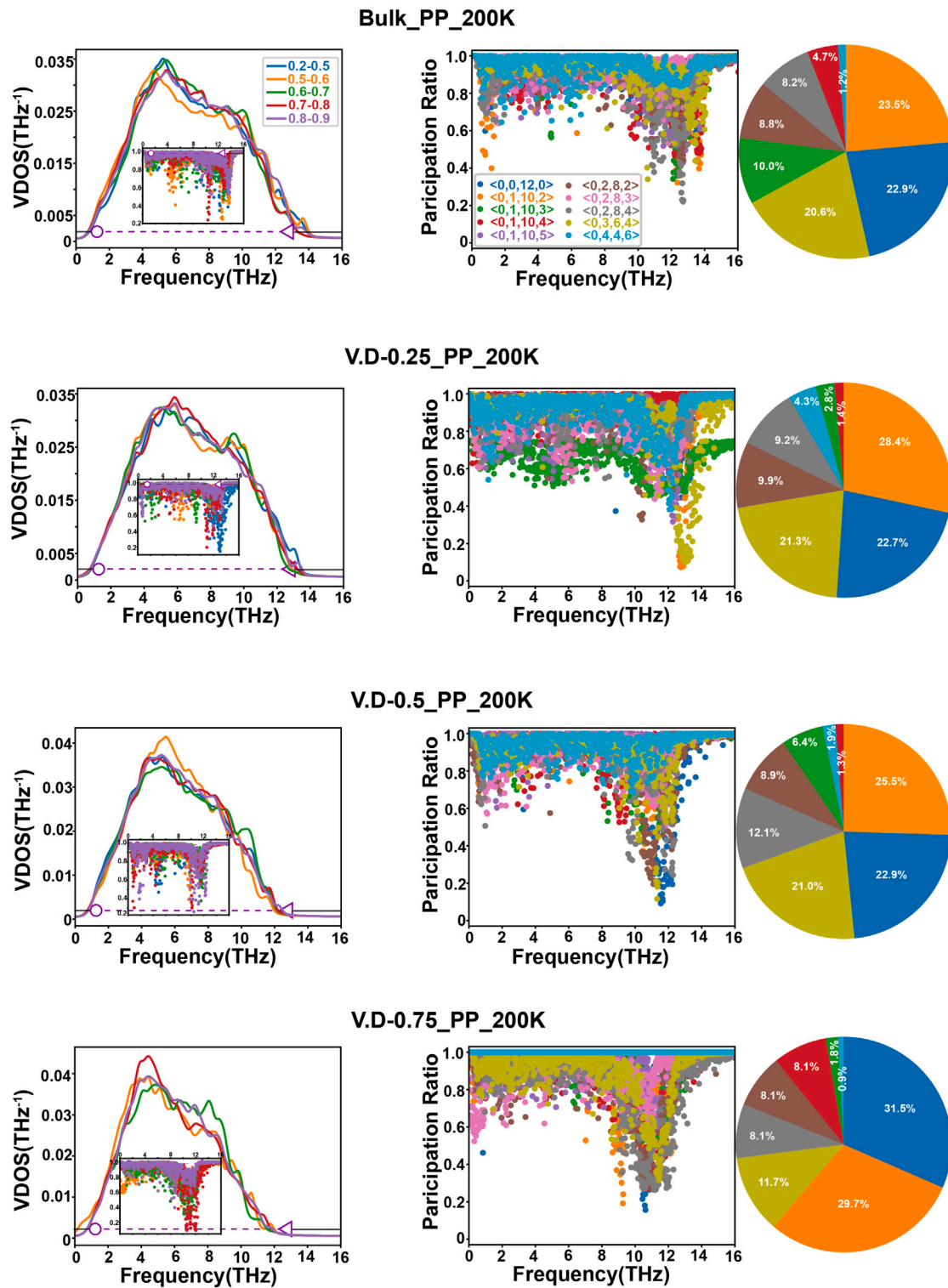


Fig. 11. The VDOS plots (left) of the selected atoms in a shell-wise representation and the PR plots (right) of the atoms creating SROs are shown for the bulk system and systems with voids in 0.25, 0.5, and 0.75 diameters at 200 K and under PP. The insets in the left plots show the corresponding PRs for the studied atoms selected in a shell-wise manner. The pie plots represent the distribution of SROs in the system, with SROs shown in the same color as used for each SRO's PR plot on the right.

ductivity was calculated by the Green-Kubo method. The possibility of tailoring the thermal conductivity was explored by introducing nanostructured voids and the stability of the structures with voids was checked. We find that the thermal conductivity decreases as a function of the porosity of the glass but not as a function of the void size. Moreover, our calculated thermal conductivities lie within a range defined

by the two limits of the Russell brick model. For a certain porosity, the atomic structural details determine the thermal conductivity relative to the Brick model limits. Finally, we have analyzed the vibrational modes and corresponding participation ratios to establish a relationship between increasing localized vibrational modes and decrease in thermal conductivity with the size of the voids.

CRediT authorship contribution statement

Emel Gürbüz: Conceptualization, Calculations, Analysis, Writing – original draft. **Biplab Sanyal:** Conceptualization, Supervision, Analysis, Writing – original draft, Funding acquisition.

Declaration of competing interest

No conflict of interest exists. We wish to confirm that there are no known conflicts of interest associated with this publication and there has been no significant financial support for this work that could have influenced its outcome.

Data availability

Data will be made available on request.

Acknowledgments

B. S. acknowledges financial support from Swedish Research Council (grant no. 2022-04309) and Energimyndigheten, Sweden (Diary no. 2018-004434 & Project number 46621-1) and Swedish Research Links programme grant (2017-05447). The computations were enabled in project SNIC 2022/3-30 by resources provided by the Swedish National Infrastructure for Computing (SNIC) at NSC, PDC, and HPC2N partially funded by the Swedish Research Council (Grant No. 2018-05973). B.S. acknowledges allocation of supercomputing hours by PRACE DECI-17 project 'Q2Dtopomat' in Eagle supercomputer in Poland and EuroHPC resources in Karolina supercomputer in Czech Republic.

Funding

1. Financial support from Swedish Research Council (grant no. 2022-04309)
2. Financial support from Energimyndigheten (Diary no. 2018-004434 & Project number 46621-1)
3. Financial support from Swedish Research Links programme grant (2017-05447)
4. High performance computation allocation from Swedish National Infrastructure for Computing (SNIC) (project number SNIC 2022/3-30)
5. High performance computation allocation from PRACE DECI-17 project 'Q2Dtopomat' in Eagle supercomputer in Poland
6. High performance computation allocation from EuroHPC resources in Karolina supercomputer in Czech Republic

References

- [1] W. Jr. Klement, R.H. Willens, P. Duwez, Non-crystalline structure in solidified Gold-Silicon alloys, *Nature* 187 (1960) 869.
- [2] Y. Liu, J. Liu, S. Sohn, Y. Li, J.J. Cha, J. Schroers, Metallic glass nanostructures of tunable shape and composition, *Nature Commun.* 6 (2015) 7043.
- [3] G. Kumar, A. Desai, J. Schroers, Bulk metallic glass: The smaller the better, *Adv. Mater.* 23 (2011) 461.
- [4] H.J. Fecht, G. Han, Z. Fu, W.L. Johnson, Metastable phase formation in the Zr-Al binary system induced by mechanical alloying, *J. Appl. Phys.* 67 (1990) 1744.
- [5] M.D. Demetriou, M.E. Launey, G. Garrett, J.P. Schramm, D.C. Hofmann, W.L. Johnson, R.O. Ritchie, A damage-tolerant glass, *Nature Mater.* 10 (2011) 123.
- [6] Y.Q. Cheng, H.W. Sheng, E. Ma, Relationship between structure, dynamics, and mechanical properties in metallic glass-forming alloys, *Phys. Rev. B* 78 (2008) 014207.
- [7] W. Zhou, Y. Cheng, K. Chen, G. Xie, T. Wang, G. Zhang, Thermal conductivity of amorphous materials, *Adv. Funct. Mater.* 30 (2020) 1903829.
- [8] David G. Cahill, S.K. Watson, R.O. Pohl, Lower limit to the thermal conductivity of disordered crystals, *Phys. Rev. B* 46 (1992) 6131–6140.
- [9] Ashutosh Giri, Brian F. Donovan, Patrick E. Hopkins, Localization of vibrational modes leads to reduced thermal conductivity of amorphous heterostructures, *Phys. Rev. Mater.* 2 (2018) 056002.
- [10] M. Beekman, D.G. Cahill, Inorganic crystals with glass-like and ultralow thermal conductivities, *Cryst. Res. Technol.* 52 (2017) 1700114.
- [11] J. Song, X. Feng, Y. Huang, Mechanics and thermal management of stretchable inorganic electronics, *Natl. Sci. Rev.* 3 (2016) 128.
- [12] S.-H. Bae, R. Shabani, J.-B. Lee, S.-J. Baeck, H.J. Cho, J.-H. Ahn, Fully current-based sub-bandgap optoelectronic differential ideality factor technique and extraction of subgap DOS in amorphous semiconductor TFTs, *IEEE Trans. Electron. Devices* 61 (2014) 3566.
- [13] K.-H. Kim, S. Hyun Jo, S. Gaba, W. Lu, Nanoscale resistive memory with intrinsic diode characteristics and long endurance, *Appl. Phys. Lett.* 96 (2010) 053106.
- [14] Y. Lu, A. Alvarez, C.-H. Kao, J.-S. Bow, S.-Y. Chen, I.-W. Chen, An electronic silicon-based memristor with a high switching uniformity, *Nat. Electron.* 2 (2019) 66.
- [15] M. Yamasaki, S. Kagao, Y. Kawamura, Thermal diffusivity and conductivity of $Zr_{55}Al_{10}Ni_5Cu_{30}$ bulk metallic glass, *Scr. Mater.* 53 (2005) 63.
- [16] C.-C. Yu, H.-J. Wu, P.-Y. Deng, M.T. Agne, G.J. Snyder, J.P. Chu, Thin-film metallic glass: an effective diffusion barrier for Se-doped $AgSbTe_2$ thermoelectric modules, *Sci. Rep.* 7 (2017) 45177.
- [17] R.Y. Umetsu, R. Tu, T. Goto, Thermal and electrical transport properties of Zr-based bulk metallic glassy alloys with high glass-forming ability, *Mater. Trans.* 53 (2012) 1721.
- [18] G. Soye, J.A. Eastman, L.J. Thompson, G.-R. Bai, P.M. Baldo, A.W. McCormick, R.J. DiMelfi, M.F. Elmustafa, D.S. Stone, Grain-size-dependent thermal conductivity of nanocrystalline yttria-stabilized zirconia films grown by metal-organic chemical vapor deposition, *Appl. Phys. Lett.* 77 (2000) 1155.
- [19] J. Chen, J.H. Walther, P. Koumoutsakos, Strain engineering of kapitza resistance in few-layer graphene, *Nano Lett.* 14 (2014) 819.
- [20] N.G. Dou, R.A. Jagt, C.M. Portela, J.R. Greer, A.J. Minnich, Ultralow thermal conductivity and mechanical resilience of architected nanolattices, *Nano Lett.* 18 (2018) 4755.
- [21] G. Henson, C.S. Jone, Materials for Launch Vehicle Structures, Invariant Labs Publication, Westlake, OH, 2018.
- [22] W.O. Soboyejo, J. Obayemi, E. Annan, E. Ampaw, L. Daniels, N. Rahbar, Review of high temperature ceramics for aerospace applications, *Adv. Mater. Res.* 1132 (2015) 385.
- [23] D.A. Bennett, R.D. Horansky, A. Hoover, N. Hoteling, M. Rabin, D. Schmidt, L. Swetz, J. Ullom, An analytical model for pulse shape and electrothermal stability in two-body transition-edge sensor microcalorimeters, *Appl. Phys. Lett.* 97 (2010) 102504.
- [24] T. Mori, Novel principles and nanostructuring methods for enhanced thermoelectrics, *Small* 13 (2017) 1702013.
- [25] D.S. Mukhopadhyay, B.C. Sales, A.A. Purotzky, M.A. McGuire, L. Lindsay, Two-channel model for ultralow thermal conductivity of crystalline Tl_3VSe_4 , *Science* 360 (2018) 1455.
- [26] W.-X. Zhou, K.-Q. Chen, First-principles determination of ultralow thermal conductivity of monolayer WSe_2 , *Sci. Rep.* 5 (2015) 15070.
- [27] Hossein Honarvar, Mahmoud I. Hussein, Spectral energy analysis of locally resonant nanophononic metamaterials by molecular simulations, *Phys. Rev. B* 93 (2016) 081412.
- [28] R. Anufriev, R. Yanagisawa, M. Nomura, Aluminium nanopillars reduce thermal conductivity of silicon nanobeams, *Nanoscale* 9 (2017) 39.
- [29] M. Nomura, J. Nakagawa, J. Kage, D. Moser, O. Paul, Thermal phonon transport in silicon nanowires and two-dimensional phononic crystal nanostructures, *Appl. Phys. Lett.* 106 (2015) 143102.
- [30] G. Romano, A.M. Kolpak, Thermal anisotropy enhanced by phonon size effects in nanoporous materials, *Appl. Phys. Lett.* 110 (2017) 093104.
- [31] B. Fu, G.H. Tang, C. Bi, Thermal conductivity in nanostructured materials and analysis of local angle between heat fluxes, *J. Appl. Phys.* 116 (2014) 124310.
- [32] G. Romano, J.C. Grossman, Toward phonon-boundary engineering in nanoporous materials, *Appl. Phys. Lett.* 105 (2014) 033116.
- [33] D.L. Cocemasov, V.M. Fomin, D. Grimm, O.G. Schmidt, Phonon-engineered thermal transport in Si wires with constant and periodically modulated cross-sections: A crossover between nano- and microscale regimes, *Appl. Phys. Lett.* 107 (2015) 011904.
- [34] J. Maire, R. Anufriev, T. Hori, J. Shiomi, S. Volz, M. Nomura, Thermal conductivity reduction in silicon fishbone nanowires, *Sci. Rep.* 8 (2018) 4452.
- [35] A.L. Moore, S.K. Saha, R.S. Prasher, L. Shi, Phonon backscattering and thermal conductivity suppression in sawtooth nanowires, *Appl. Phys. Lett.* 93 (2008) 083112.
- [36] C. Blanc, A. Rajabpour, S. Volz, T. Fournier, O. Bourgeois, Phonon heat conduction in corrugated silicon nanowires below the Casimir limit, *Appl. Phys. Lett.* 103 (2013) 043109.
- [37] A.P. Gonçalves, E.B. Lopes, O. Rouleau, C. Godart, Conducting glasses as new potential thermoelectric materials: the Cu–Ge–Te case, *J. Mater. Chem.* 20 (2010) 1516.
- [38] K.H.J. Buschow, P.H. Smit, Magnetic and electrical transport-properties of amorphous Zr-Fe alloys, *J. Magn. Magn. Mater.* 23 (1981) 85.
- [39] S. Plimpton, Fast parallel algorithms for short-range molecular-dynamics, *J. Comput. Phys.* 117 (1995) 1.
- [40] J. Cai, Y.Y. Ye, Simple analytical embedded-atom-potential model including a long-range force for fcc metals and their alloys, *Phys. Rev. B* 54 (1996) 8398–8410.

- [41] G. Kresse, J. Hafner, Ab initio molecular-dynamics simulation of the liquid-metal-amorphous-semiconductor transition in germanium, *Phys. Rev. B* 49 (1994) 14251–14269.
- [42] G. Kresse, J. Furthmüller, Efficiency of ab-initio total energy calculations for metals and semiconductors using a plane-wave basis set, *Comput. Mater. Sci.* 6 (1996) 15.
- [43] P.E. Blöchl, Projector augmented-wave method, *Phys. Rev. B* 50 (1994) 17953–17979.
- [44] John P. Perdew, Kieron Burke, Matthias Ernzerhof, Generalized gradient approximation made simple, *Phys. Rev. Lett.* 77 (1996) 3865–3868.
- [45] H.J. C. Berendsen, J.P. M. Postma, W.F. van Gunsteren, A. Dinola, J.R. Haak, Molecular-dynamics with coupling to an external bath, *J. Chem. Phys.* 81 (1984) 3684.
- [46] Jun Kang, Lin-Wang Wang, First-principles Green-Kubo method for thermal conductivity calculations, *Phys. Rev. B* 96 (2017) 020302.
- [47] A. Kinaci, J.B. Haskins, T. Çağın, On calculation of thermal conductivity from Einstein relation in equilibrium molecular dynamics, *J. Chem. Phys.* 137 (2012) 014106.
- [48] R. Kubo, Statistical-mechanical theory of irreversible processes .I. General theory and simple applications to magnetic and conduction problems, *J. Phys. Soc. Japan* 12 (1957) 570.
- [49] R. Zwanzig, Time-correlation functions and transport coefficients in statistical mechanics, *Annu. Rev. Phys. Chem.* 16 (1965) 67.
- [50] Patrick K. Schelling, Simon R. Phillpot, Pawel Keblinski, Comparison of atomic-level simulation methods for computing thermal conductivity, *Phys. Rev. B* 65 (2002) 144306.
- [51] A.P. Thompson, S.J. Plimpton, W. Mattson, General formulation of pressure and stress tensor for arbitrary many-body interaction potentials under periodic boundary conditions, *J. Chem. Phys.* 131 (2009) 154107.
- [52] A.J. H. McGaughey, M. Kaviany, Thermal conductivity decomposition and analysis using molecular dynamics simulations. Part I. Lennard-Jones argon, *Int. J. Heat Mass Transfer* 47 (2004) 1783.
- [53] M. Zhou, T. Liang, B. Wu, J. Liu, P. Zhang, Phonon transport in antisite-substituted hexagonal boron nitride nanosheets: A molecular dynamics study, *J. Appl. Phys.* 128 (2020) 234304.
- [54] F. DeAngelis, M.G. Muraleedharan, J. Moon, R.S. Seyf, A.J. Minnich, A.J. H. McGaughey, H. Asegun, Thermal transport in disordered materials, *Nanosc. Microsc. Therm. Eng.* 23 (2019) 81.
- [55] R.S. Seyf, A.J. H. McGaughey, H. Asegun, A method for distinguishing between propagons, diffusions, and locons, *J. Appl. Phys.* 120 (2016) 025101.
- [56] R. Zallen, *The Physics of Amorphous Solids*, Wiley-VCH Weinheim, 2004.
- [57] C.C. Wang, K.J. Dong, A.B. Yu, Analysis of voronoi clusters in the packing of uniform spheres, *AIP Conf. Proc.* 1542 (2013) 353.
- [58] S.H. Wu, G.Q. Guo, J.G. Wang, L. Yang, Structural mechanism of the enhanced glass-forming ability in multicomponent alloys with positive heat of mixing, *Sci. Rep.* 6 (2016) 38098.
- [59] L. Yang, H.Y. Li, P.W. Wang, S.Y. Wu, G.Q. Guo, B. Liao, Q.L. Guo, X.Q. Fan, P. Huang, H.B. Lou, F.M. Guo, Q.S. Zeng, T. Sun, Y. Ren, L.Y. Chen, Structural responses of metallic glasses under neutron irradiation, *Sci. Rep.* 7 (2017) 16739.
- [60] H.W. Russell, Principles of heat flow in porous insulators, *Amer. Ceram. Soc.* (1934) 1.
- [61] Syoten Oka, Kuniko Yamane, Theory of the conduction of heat in foamed plastics, *Japan. J. Appl. Phys.* 6 (1967) 469.
- [62] Lv. Wei, H. Asegun, Non-negligible contributions to thermal conductivity from localized modes in amorphous silicon dioxide, *Sci. Rep.* 6 (2016) 35720.